



## Evaluating the self-healing capacity of textile-derived cellulose in cementitious composites

Chamini Liyanage , Chamila Gunasekara , Magdalena Rajczakowska , David W. Law & Sujeeva Setunge

To cite this article: Chamini Liyanage , Chamila Gunasekara , Magdalena Rajczakowska , David W. Law & Sujeeva Setunge (11 May 2026): Evaluating the self-healing capacity of textile-derived cellulose in cementitious composites, Journal of Sustainable Cement-Based Materials, DOI: [10.1080/21650373.2026.2671347](https://doi.org/10.1080/21650373.2026.2671347)

To link to this article: <https://doi.org/10.1080/21650373.2026.2671347>



© 2026 The Author(s). Published by Informa UK Limited, trading as Taylor & Francis Group



Published online: 11 May 2026.



Submit your article to this journal [↗](#)



Article views: 75



View related articles [↗](#)



View Crossmark data [↗](#)

## Evaluating the self-healing capacity of textile-derived cellulose in cementitious composites

Chamini Liyanage<sup>a</sup>, Chamila Gunasekara<sup>a\*</sup>, Magdalena Rajczakowska<sup>b</sup>, David W. Law<sup>a</sup> and Sujeeva Setunge<sup>a</sup>

<sup>a</sup>Civil & Infrastructure Engineering, School of Engineering, RMIT University, Melbourne, Australia; <sup>b</sup>Department of Civil, Environmental and Natural Resources Engineering, Luleå University of Technology, Luleå, Sweden

(Received 6 March 2026; Accepted 5 May 2026)

Cracking remains a primary durability challenge in concrete infrastructure, particularly in water-retaining and marine environments. This study evaluates recycled textile-derived cellulose as a sustainable self-healing agent for cementitious composites. Specimens with 0–5% cellulose replacement underwent controlled surface cracking and internal mechanical damage, with healing quantified over 28 days *via* optical microscopy, micro-CT, mechanical testing, and microstructural characterization. Results demonstrated that 2% cellulose incorporation was the optimum dosage, enhancing both surface and internal healing. Surface crack closure was 10.46% for narrow cracks and 4.87% for the control, while internal healing efficiency achieved 22.1% compared to 11.8% for plain mortar. Micro-CT revealed a 61.2% reduction in elongated crack-like voids, and compressive strength recovery peaked at 123.5%. SEM/EDS identified C-S-H, calcium carbonate, and calcium hydroxide precipitation, driven by cellulose-mediated internal curing and fiber bridging. The hydrophilic cellulose network sustains crack repair through internal moisture retention, without external healing agents.

**Keywords:** Cellulose; cement; crack; micro-CT; microscopy; self-healing

### 1. Introduction

Owing to the multiple beneficial characteristics of concrete, including durability, strength, adaptability, fire resistance, cost-effectiveness, thermal mass, widespread availability, and straightforward production, it remains the most used construction material in the world. However, concrete requires steel reinforcement to compensate for its inherent weakness in resisting tensile forces. Despite careful design and construction, concrete inevitably develops cracks from temperature variations, excess water, shrinkage, fatigue loads, and structural settlement. These cracks can significantly undermine the durability of the structure by allowing gases and liquids to infiltrate and even result in the corrosion of the reinforcement [1]. The consequences are especially severe in critical infrastructure such as water-retaining structures, underground facilities, and marine environments, where watertightness and long-term durability are essential. Repairing micro-cracks in such structures is both costly and disruptive, making enhanced autogenous healing an attractive alternative. Developing concrete with improved self-healing capacity through sustainable bio-based additives, therefore offers significant potential for reducing long-term maintenance costs and extending structural service life.

Concrete healing mechanisms are of two kinds: autogenous and autonomous. Autogenous healing relies solely on the chemical reactions of the cementitious materials to repair cracks, requiring no external agents. Meanwhile, autonomous healing incorporates external

substances such as bacteria, calcium lactate, or fly ash to enhance the healing of cracks in the concrete surface [2,3]. Healing methods include chemical encapsulation systems, where microcapsules containing chemicals rupture upon damage, releasing agents to flow and cure within the crack [4], microbial additives that promote crack sealing through biogenic calcium carbonate deposition [5], and the incorporation of mineral admixtures (supplementary cementitious materials) or expansive components that promote continued hydration and volume increase to close cracks [4,6].

In light of the increasing emphasis on sustainable construction materials, bio-based healing agents have emerged as a research priority. Cellulose, as an abundant and renewable biomaterial, offers considerable potential for self-healing applications in cement composites, forming the focus of the present study. Previous research studies have demonstrated that cellulose incorporation in cement composites not only enhances mechanical strength [7–9], reduces porosity [8] and exhibits lower toxicity [8], but also improves resistance to cracking [10–13]. Singh and Gupta [14] studied the self-healing efficiency of cellulose in concrete and observed that the incorporation of 0.5% cellulose increased the rate of healing. Cracking in the plastic shrinkage phase can be reduced by 85% with cellulose fibers compared to conventional concrete due to their ability to restrict crack width. Due to the hydrophilic nature of cellulose, they can promote internal curing, such that the availability of moisture helps in the crack healing.

\*Corresponding author. Email: [chamila.gunasekara@rmit.edu.au](mailto:chamila.gunasekara@rmit.edu.au)

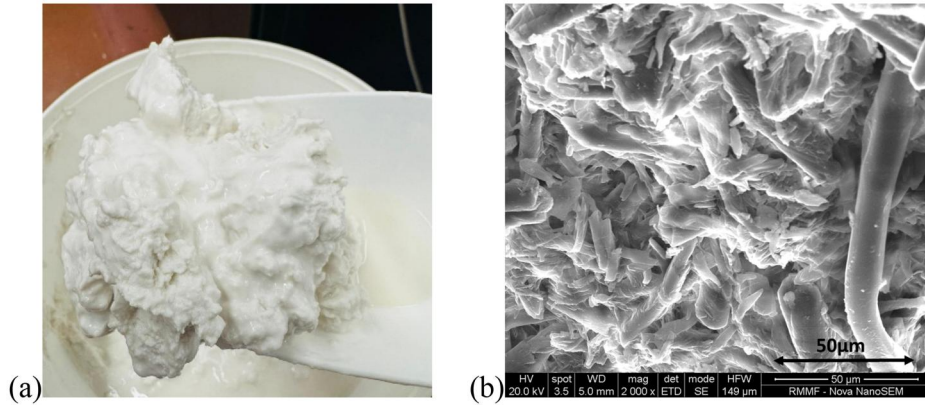


Figure 1. Recycled textile cellulose: (a) physical appearance and (b) microscopic view.

Additionally, the alkali resistance of cellulose causes continued hydration and thus, the cracks are also filled through additional crystallization [14]. The alkali resistance is primarily due to the removal of amorphous components, specifically lignin and hemicellulose, during fiber processing [15,16]. Unlike raw natural fibers, which are susceptible to hydrolysis and degradation in the high-pH cementitious environment, the processed cellulose maintains structural integrity [17,18]. Consequently, the fibers remain stable to function as internal moisture reservoirs, sustaining the release of water to drive the long-term hydration and carbonation reactions required for healing [14,19]. The effectiveness of this chemical recovery is closely tied to the physical morphology of the cellulose used.

Beyond these material enhancements, cellulose is strategically employed as a component in extrinsic self-healing systems. Specifically, these natural cellulose fibers are used as a protective carrier for bacteria and calcium lactate nutrients. This bio-mediated approach exploits the porosity of fibers and their role as a bridge across the crack face to maximize the effectiveness of microbiologically induced precipitation of calcite. Experimental quantification of the autonomous bio-healing system, utilizing cellulose fibers as protective carriers for *Bacillus subtilis* bacteria, demonstrated significant potency, achieving self-healing ratios up to 98.3% based on ultrasonic pulse velocity [20]. Furthermore, microcrystalline cellulose, originating from refined wood or vegetable pulp has been successfully incorporated into healing capsules to provide volumetric expansion *via* water-induced swelling. This physical expansion, combined with water retention and the bridging effects of fibers, facilitates the precipitation of healing products, enabling the sealing of cracks up to 500  $\mu\text{m}$  [21].

Existing cellulose-based self-healing research, whether utilizing wood-derived fibers for autogenous healing or natural plant fibers as biological carriers, predominantly relies on virgin sources or primary industrial by-products, including sisal, coconut fibers, and sugar beet pulp. While these natural fibers are effective, they represent a consumption of primary resources. Unlike these natural fibers, which retain lignin and hemicellulose and are susceptible to alkaline degradation in the cementitious environment [15,22], the recycled textile cellulose investigated

here has undergone processing to remove these components, resulting in higher crystallinity, higher thermal stability and higher C/O ratio [23] and is expected to support a more stable and consistent healing performance [21]. Despite growing emphasis on circular economy principles, the self-healing capacity of post-consumer recycled cellulose remains unexplored for concrete applications. This represents a critical knowledge gap, as large-scale textile recycling streams offer abundant, sustainable cellulose. The present investigation addresses this deficiency by systematically evaluating the self-healing characteristics of cellulose extracted from recycled cotton waste textiles in cement paste and mortar, establishing a foundation for integrating secondary material resources into infrastructure repair systems.

Importantly, the healing mechanism explored in the present study is fundamentally distinct from extrinsic strategies such as microbially induced calcite precipitation (MICP) and encapsulation-based systems, which rely on externally introduced agents. Instead, the recycled textile cellulose functions as an intrinsic moisture reservoir, sustaining autogenous crack sealing through prolonged hydration and carbonation reactions driven entirely by water released from within the fiber structure.

## 2. Experimental program

### 2.1. Materials

Australian General-Purpose Cement, adhering to AS 3972-2010 standard [24] was utilized as the primary binder. The study incorporated recycled cellulose derived from waste cotton textiles, sourced from a commercial manufacturer (Blocktexas). The cellulose was available in the form of an aqueous suspension with a 0.64 moisture content, determined gravimetrically by oven-drying at 105  $^{\circ}\text{C}$  to constant mass. The cellulose exhibited particle sizes principally between 10 and 30  $\mu\text{m}$ , comparable to standard cement particles, as characterized by laser diffraction. Figure 1 shows the physical appearance and a scanning electron microscopic image of the cellulose. The C/O ratio, of 1.05, was obtained from EDS point analysis, and crystallinity of 59% was determined by XRD analysis. Uncrushed river sand, according to ASTM C33/

Table 1. Mix proportions of materials for paste and mortar mixtures (kg/m<sup>3</sup>).

Mix ID	Cement	Cellulose	Sand	Water
P0	1394	0.0	0	558
P1	1380	13.9	0	558
P2	1366	27.9	0	558
P5	1324	69.7	0	558
M0	539	0.0	1482	270
M1	534	5.4	1482	270
M2	528	10.8	1482	270
M5	512	26.9	1482	270

C33M [25] was utilized as the fine aggregate in mortar samples. Tap water was used throughout the sample preparation.

## 2.2. Mix design and sample preparation

To evaluate cracking behavior in cellulose-cement composites, both cement paste and mortar specimens were fabricated. Paste specimens enabled clear observation of surface crack healing under optical microscopy due to their smooth, homogeneous surface, while mortar specimens were used for internal crack evaluation, as their larger void structures and crack volumes are detectable *via* micro-CT scanning. The two specimen types were intentionally selected to represent complementary damage scenarios, surface plastic shrinkage cracking and internal mechanical damage, each requiring a matrix and crack-induction method best suited to the respective healing measurement. Although the two series differ in specimen type and crack generation method, the cellulose replacement levels are identical.

In both series, all mix proportions are expressed on a dry cellulose mass basis, with cellulose content defined as a percentage replacement of cement by dry weight. In practice, cellulose was introduced in the slurry form supplied in all formulations, and the water contained in the slurry was incorporated within the total reported water content for each mix. As cellulose replaces cement without equivalent binder contribution, the effective water-to-binder ratio increases slightly with increasing cellulose dosage in both series (from 0.40 to 0.42 in paste and from 0.50 to 0.52 in mortar), a minor but consistent compositional variable inherent to the replacement methodology adopted.

### 2.2.1. Cement paste specimens

Four paste formulations (P0, P1, P2, P5) were prepared with 0%, 1%, 2%, and 5% cellulose replacement by weight of cement, respectively. The control mix (P0) maintained a water/cement ratio of 0.4, while other mixes were obtained by replacing 1%, 2% and 5% of the cement with cellulose (Table 1). The mixing procedure involved initial hand mixing of all the materials for 2 min, followed by mechanical mixing of 4 min at 1000 rpm, employing a planetary centrifugal mixer (THINKY ARV-310, Japan). Freshly prepared paste was cast into circular disc-shaped

molds measuring 8 cm in diameter and 1 cm in depth, with specimens tamped for 30 s to eliminate entrapped air.

### 2.2.2. Mortar specimens

Mortar mixtures (M0, M1, M2 and M5) were prepared, maintaining the same cellulose dosages as the paste samples, with mix proportions provided in Table 1. The control mixture (M0) maintained a water/cement ratio of 0.5 and a sand/cement ratio of 2.75 by weight [26]. The mortar preparation procedure employed a mechanical mortar mixer with a paddle. Cement was first mixed with 75% of the total water at 140 rpm for 30 s. Prior to addition, the cellulose slurry was pre-mixed with the remaining 25% of the mix water to achieve uniform dispersion before incorporation into the mortar. The mixer was stopped for 90 s to collect all the materials into the center of the bowl. All the materials were mixed for another 60 s at a speed of 285 rpm [27]. The fresh mortar was immediately transferred to 25 mm cubic molds and vibrated using a vibrating table for 30 s to ensure uniform compaction.

## 2.3. Crack formation and curing

Crack induction methods employed in this study targeted both surface and internal damage. Specifically, plastic shrinkage cracks were induced on the top surface of the paste samples, while internal cracks were mechanically introduced within the mortar samples, based on the reported methodology from existing literature [28].

### 2.3.1. Paste cracks

Freshly prepared paste samples were initially kept at room conditions ( $23 \pm 2^\circ\text{C}$  temperature) for 2 h after casting and then exposed to direct sunlight (temperature of  $28 \pm 2^\circ\text{C}$ ) for 2 h during the midday period (12.00–14.00) to induce plastic shrinkage cracks on the top surface of the samples (Figure 2a,b). Samples underwent an additional 18-hour curing at room conditions before demoulding. The samples were then transferred to a controlled atmosphere ( $23 \pm 2^\circ\text{C}$  and 90–95% RH) for continued curing, with crack width observation carried out at different ages.

### 2.3.2. Mortar cracks

After the preparation of mortar samples, they underwent initial curing at ambient temperature ( $23^\circ\text{C}$ ) for 24 h before demoulding. Samples were then transferred to water for an additional 2 days of continued curing. At this stage, samples were removed from water, allowed to air-dry for 3 h, and a subset was tested for compressive strength. For crack induction, remaining samples were wrapped with duct tape on the outer surfaces of the sample, except the top and bottom, (Figure 3a) and 90% of the breaking load of each mixture was applied on these samples (Figure 3b). This mix-normalised loading approach was adopted to ensure proportionally equivalent damage states across formulations with different compressive strengths, consistent with established protocols [28,29]. Applying a fixed absolute load across all mixes

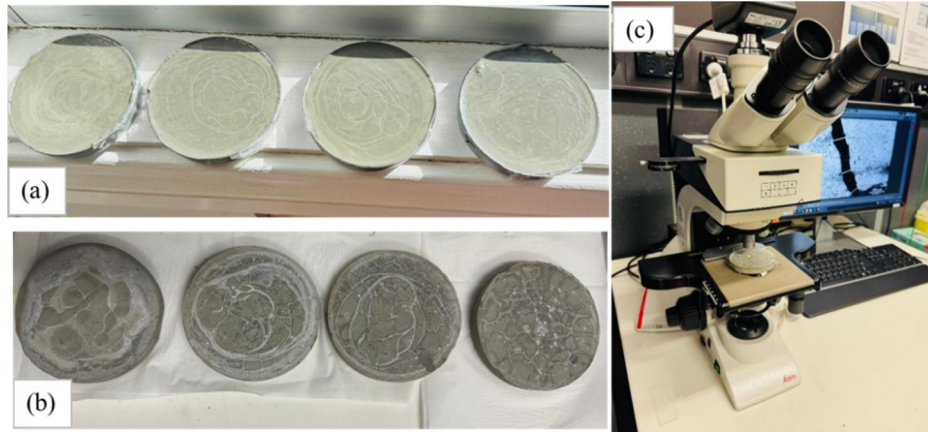


Figure 2. Paste samples: (a) inducing shrinkage cracks, (b) with cracks, and (b) microscopic observation.

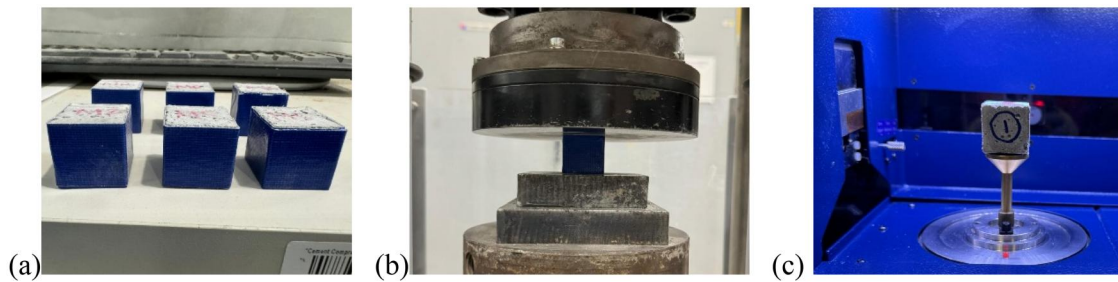


Figure 3. Mortar samples: (a) wrapped with duct tape, (b) creating cracks, and (c) micro-CT scanning.

would have produced disproportionate damage in weaker formulations, compromising the comparability of healing measurements. The resulting damage states were verified through 0-day post-cracking micro-CT scans, which confirmed internal crack formation across all mixes at a consistent level of severity. The cracked specimens remained under controlled curing ( $23 \pm 2^\circ\text{C}$ , 90–95% RH) throughout the study, with tests performed at specified ages.

## 2.4. Evaluation of self-healing capacity

### 2.4.1. Microscopic observation

Cracked surfaces of the paste samples were examined using an optical microscope (Leica DM 2500, Germany), at 1, 3, 7, 14 and 28 days post-casting (Figure 2c). Before testing, each sample was air-dried for a few minutes to remove any surface moisture. One specimen per mix proportion was monitored for surface cracks. Five crack locations were identified on each specimen, based on crack widths falling within the target range of 100–250  $\mu\text{m}$ , identified during the initial observation day. Locations were selected to be spatially distributed across the specimen surface rather than clustered, ensuring representative coverage of the cracked area. Three points along each crack were measured, yielding 15 measurements per specimen per time point, from which average healing efficiency values were calculated. To minimize operator bias, the selected crack locations were physically marked on the specimen at initial measurement, and the same locations were revisited at each subsequent observation age, and all measurements were performed by the same

operator throughout the testing period to ensure consistency. Leica Application Suite X (LAS X) was utilized for image processing and crack width measurement. Healing efficiency of the cracks in paste samples was evaluated using Equation (1) [21].

$$\text{Healing efficiency of surface cracks (\%)} = \frac{W_1 - W_2}{W_1} \times 100\% \quad (1)$$

where  $W_1$  and  $W_2$  are initial crack width and final crack widths for the specific time period considered. After the 28-day crack monitoring, samples were subjected to Scanning Electron Microscopy (SEM). Paste samples were cut into a size of  $10 \times 10 \times 10 \text{ mm}^3$  with the undisturbed top surface and sputtered with 5 nm of Palladium to suppress charging. FEI Quanta 200 Scanning Electron Microscope, with secondary electron and an Energy-dispersive X-ray spectroscopy (EDS) detector, was utilized to observe and identify the elements in the cracked locations. An accelerating voltage of 15 kV with a spot size of 5 was used during the test. EDS results were analyzed using AZtec-4.3 software.

### 2.4.2. Micro-CT scanning

Mortar samples were subjected to micro-CT scanning (Figure 3c), employing a micro-CT scanner (Bruker SkyScan1275, Belgium). For each mix formulation, one specimen was subjected to repeated micro-CT scanning at all time points. The use of a single specimen per mix for scanning is consistent with the methodology adopted in prior self-healing studies using micro-CT [28,29], where the same specimen is re-scanned to directly track internal

Table 2. Summary of specimen replications and measurement protocols.

Test	Specimen type	Specimens per mix	Measurements per specimen	Reported metric
Surface crack measurement	Cement paste	1	15 crack width measurements (5 locations x 3 points per age)	Average healing efficiency
Internal void healing	Mortar	1	1 per age rescanned the same at each age	Porosity reduction
Compressive strength recovery	Mortar	3 per condition	1 per specimen	Average strength and recovery ratio

structural changes over time, avoiding the variability introduced by comparing different specimens with inherently different crack geometries and void distributions. Initially, scanning was conducted on undamaged 3-day-old mortar samples to define the baseline pore structure of each dosage group. To quantify the subsequent damage and restoration, the same specimens were re-scanned at intervals of 1, 3, 7, 14, and 28 days post-cracking to monitor the spatial and volumetric progression of the healing process. The scanning protocol utilized 20  $\mu\text{m}$  resolution and operational parameters of 0.5° rotation increments, 100  $\mu\text{A}$  current, 100 kV voltage and 1.00 mm thick copper filtering. Data analysis utilized Bruker and Dragonfly software packages through a systematic workflow. NRecon software was employed for image reconstruction from raw scan data, with identical reconstruction parameters applied across all scans to ensure consistency. DataViewer software then aligned images from each specimen across all testing ages to ensure consistent regions of interest for comparative analysis. Subsequently, quantitative analysis and 3D characterization were executed using Dragonfly (version 2025.1). This platform was utilized for image segmentation, crack identification, and the quantification of void characteristics. Total porosity was determined by segmenting the entire void space of the mortar specimens. Image segmentation was performed using a global grayscale threshold, determined through Otsu's method applied to the grayscale histogram of each reconstructed image. The threshold was established on the pre-damage scan of each specimen and held constant across all subsequent scans of the same specimen to ensure temporal consistency of void identification. Voids were defined as regions with grayscale values below the threshold, corresponding to air-filled pore spaces distinguishable from the denser cementitious matrix. This total void volume was then further analyzed and categorized into pores or cracks according to established geometric thresholds of the voids. Healing efficiency of the mortar samples was evaluated using the porosity measurements, using Equation (2), adopted from [30].

$$\begin{aligned} \text{Healing efficiency of internal voids (\%)} \\ = \frac{P_1 - P_2}{P_1} \times 100\% \end{aligned} \quad (2)$$

where  $P_1$  represents the porosity of cracked samples measured immediately after crack formation, and  $P_2$  represents the porosity of the same samples after the healing period. Additionally, void geometry was characterized using sphericity and aspect ratio parameters to distinguish

between pores and cracks. Sphericity is defined as the ratio of the surface area of a sphere (with the same volume as the void) to the actual surface area of the void [29], whereas the aspect ratio is determined by the ratio of the major axis length to the minor axis length [31].

### 2.4.3. Mechanical strength recovery

Mechanical strength recovery was evaluated by comparing the compressive strengths of cracked-healed specimens to those of uncracked reference specimens at equivalent age. Three specimens per mix were tested for each condition, cracked-healed and uncracked, and the reported compressive strength values represent the average of three measurements. In parallel to the cracked specimens, uncracked specimens were maintained under the same curing conditions to provide age-matched strength references. Compressive strengths of both cracked and uncracked sample sets were assessed after the healing period of 28 days, and the mechanical strength recovery was calculated using Equation (3) [21].

$$\text{Mechanical strength recovery (\%)} = \frac{S_1}{S_2} \times 100\% \quad (3)$$

where  $S_1$  represents the compressive strength of cracked-healed specimens, and  $S_2$  represents the compressive strength of uncracked specimens at the same age. This metric indicates the extent to which healing restored the load-bearing capacity of damaged mortar relative to undamaged material.

Table 2 shows the summary of specimen replications and measurement protocols adopted in each self-healing measurement.

## 3. Results and discussion

### 3.1. External healing

#### 3.1.1. Crack width observation

The evolution of surface crack healing evident in cement paste specimens over the 28-day period is visually documented in Figure 4. A comparative analysis of the micrographs reveals that while the control sample (P0) exhibited minimal autogenous healing, the cellulose-incorporated samples (P1, P2, and P5) showed a progressive reduction in crack width. Specifically, the P2 and P5 which contain 2% and 5% cellulose respectively, demonstrated the most significant visual closure. Specially, reduction of crack width in these two samples is visually observed after a 7-day period.

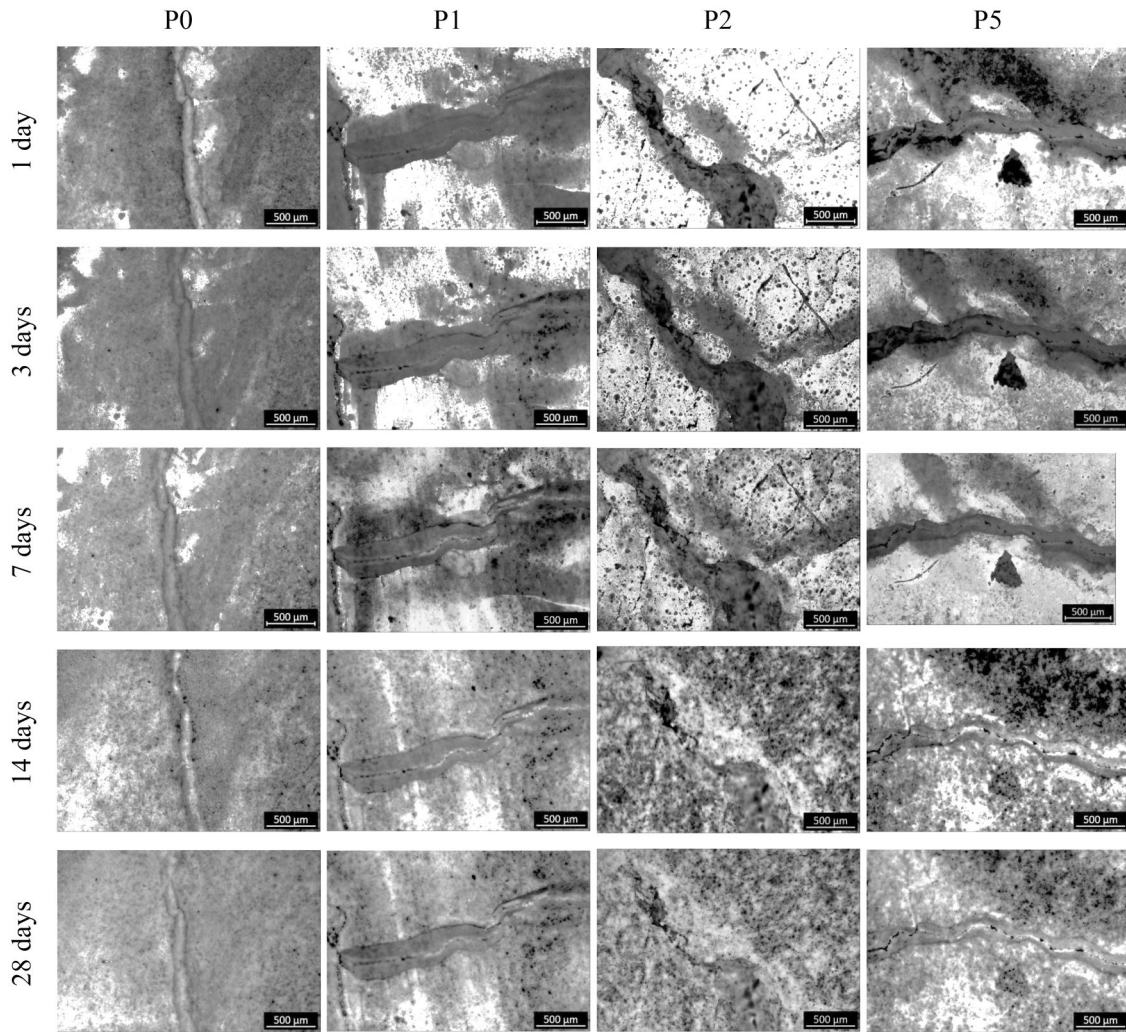


Figure 4. Evolution of surface crack width at the same measurement location in cement paste over 28 days.

Measured surface cracks were grouped by initial width into three ranges, 100–150, 150–200, and 200–250  $\mu\text{m}$ . The resulting healing efficiencies at different curing intervals are detailed in Figure 5. Based on the experimental data, it is evident that the cellulose-modified specimens (P1, P2, P5) consistently exhibited superior healing efficiency compared to the control group (P0) for all curing intervals. While P0 generally maintained a healing efficiency below 1.5% during individual intervals, inclusion of cellulose enhanced the healing by up to 3.5%. The enhanced performance was maintained irrespective of the initial crack width, suggesting that the inclusion of cellulose provides a robust mechanism for accelerating autogenous healing throughout the various stages of the 28-day curing period. The most significant healing activity occurred during the 3–7 day interval (Figure 5b), primarily for cracks within the 100–150  $\mu\text{m}$  range. During this period, P2 consistently outperformed other mixtures, achieving a superior efficiency of 3.57% for cracks between 100 and 150  $\mu\text{m}$  and 3.47% for cracks between 150 and 200  $\mu\text{m}$ .

The cumulative healing efficiency over the entire 28-day timeframe is presented in Figure 6. From the results, it is evident that across all mixtures, healing efficiency

gradually reduces as the crack width increases. For instance, in the P2 mixture, efficiency dropped from a peak of 10.46% for narrow cracks (100–150  $\mu\text{m}$ ) to 8.22% for medium cracks (150–200  $\mu\text{m}$ ) and finally to 6.86% for the widest category (200–250  $\mu\text{m}$ ).

On the other hand, in all crack width categories, the cellulose-incorporated mixtures (P1, P2, and P5) exhibited significantly higher healing efficiency than the P0 control. While the control reached a maximum of only 4.87% for narrow cracks, the cellulose-modified samples effectively doubled this capacity. Among the tested concentrations, P2 (2% cellulose) demonstrated the optimum healing efficiency regardless of the initial crack width. Peak values for P2 reached 10.46%, 8.22%, and 6.86% for the three width ranges: 100–150, 150–200, and 200–250  $\mu\text{m}$ . Interestingly, while the P5 sample (5% cellulose) also showed improved healing over the control, their efficiency, peaking at 7.36% for narrow cracks, the efficiency was lower than that of the P2 mix. This suggests that excessive fiber content may lead to dispersion challenges or localized matrix porosity that limits the effectiveness of the sealing process. Consequently, a 2% cellulose dosage appears to provide the optimal balance for moisture retention and internal curing, facilitating crack healing.

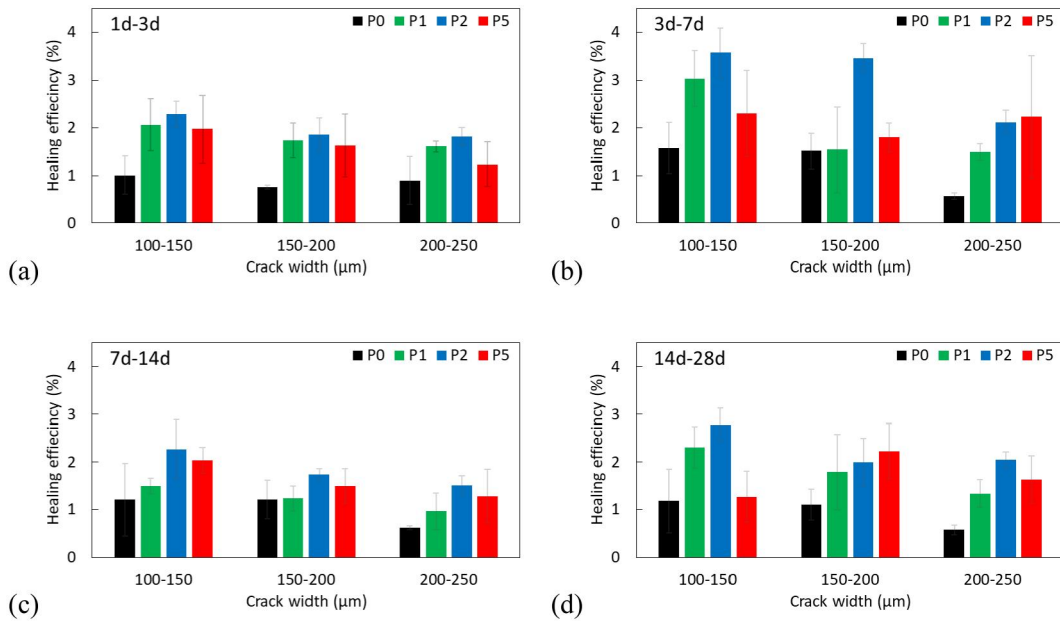


Figure 5. Healing efficiency at different curing intervals: (a) from 1 day to 3 days, (b) from 3 days to 7 days, (c) from 7 days to 14 days, and (d) from 14 days to 28 days.

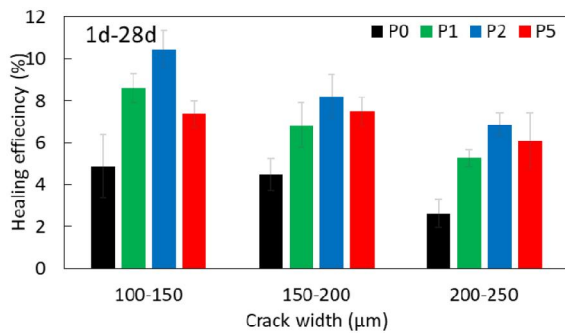


Figure 6. Healing efficiency during the whole tested time-frame (1 day to 28 days).

### 3.1.2. SEM/EDS observation

Following the 28-day curing period, SEM and EDS analyses were conducted to characterize the healing products within the crack interfaces of the cellulose-modified samples. Figure 7, Figure 8, and Figure 9 illustrate the microscopic appearance and elemental composition of the precipitates in P1, P2, and P5, respectively. Across all samples, the cracked regions were found to be partially or fully occupied by mineralized products. Microscopic examination reveals that the healing products are not uniformly distributed but are primarily concentrated at the interfaces with damage; specifically, minerals are observed to have precipitated extensively at the edges of the cracks (Figures 7b,c and 8b,c). The EDS point spectra containing atomic data, presented in Figure 10, provide quantitative elemental identification of each compound [32,33]. C-S-H is categorized at multiple locations by co-present O, Si, and Ca, consistent with C-S-H stoichiometry. CH is identified by dominant Ca and O in the complete absence of Si.  $\text{CaCO}_3$  is characterized by elevated C and Ca and negligible Si, with the relatively high C content partly attributed to adjacent cellulose contributions. Cellulose fibers are clearly distinguished from the

surrounding healing products by their dominant C content (66.6–76.1%) and trace Ca.

The microscopic evidence further highlights the role of cellulose as a localized reinforcement within the damage zones. Rather than traversing the full span of the crack, fibers are seen extending into the crack void, effectively holding segments of the matrix together, as shown in Figures 7b and 8b. Given the smaller dimension of the cellulose relative to the 100–250  $\mu\text{m}$  crack widths, direct wall-to-wall mechanical bridging by individual fibers is not observed. Rather, the fibers act as an internal scaffold suspended within the void, micro-bridging individual healing crystals to create a consolidated network that progressively bonds to both crack walls, achieving macroscopic crack sealing through a cooperative fiber-crystal mechanism [16]. These fibers act as discrete internal bridges that stabilize the crack interior, serving as localized nucleation sites for the growth of crystalline products. This partial bridging is instrumental in securing the mineralized seal within the cementitious matrix. The moisture-retaining nature of the cellulose fibers facilitates the uptake of atmospheric  $\text{CO}_2$ , which reacts with calcium hydroxide in the matrix to promote the formation of  $\text{CaCO}_3$  crystals. The EDS analysis confirms the deposition of  $\text{CaCO}_3$ , C-S-H, and CH within the mineralized zones (Figure 10), with the quantitative atomic data directly supporting their elemental identification and distinguishing each product from the surrounding cellulose fibers and cement matrix.

However, the efficacy of this mechanism is dosage dependent. In the P5 samples, evidence of agglomeration is visible as in Figure 9b,c, where the higher dosage of cellulose led to fiber clumping. This agglomeration likely hindered uniform dispersion and created localized zones of weakness, explaining the lower healing efficiency observed in the 5% mixture compared to the optimal 2% (P2) dosage. Collectively, the SEM and EDS findings

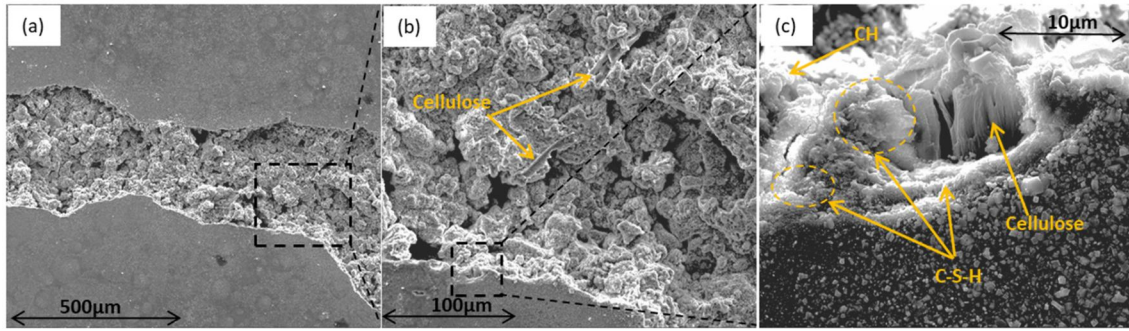


Figure 7. SEM images of P1 after 28-day healing, showing hydration products around cellulose at the crack interface, at increasing magnification levels.

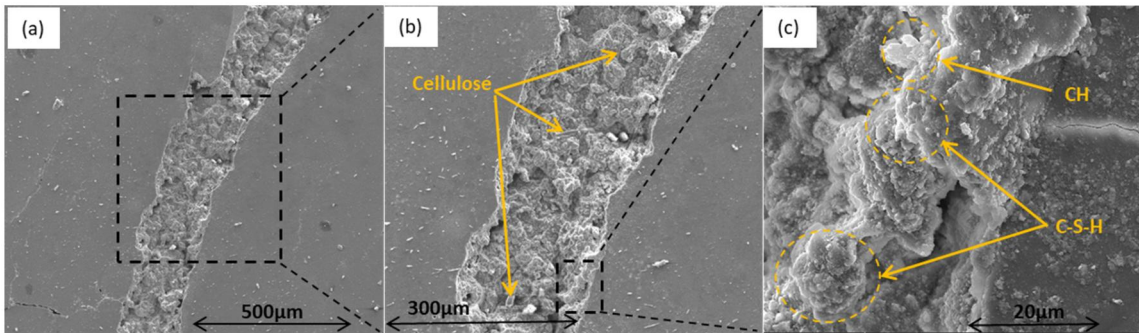


Figure 8. SEM images of P2 after 28-day healing, showing hydration products around cellulose at the crack interface, at increasing magnification levels.

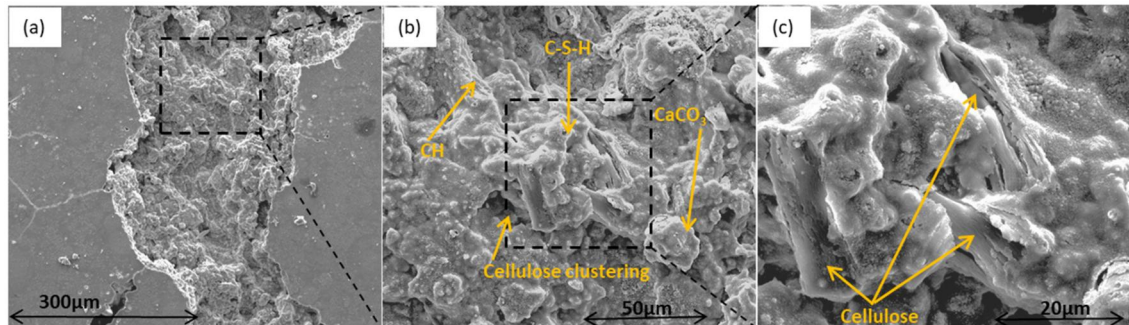


Figure 9. SEM images of P5 after 28-day healing, showing hydration products around cellulose at the crack interface, at increasing magnification levels.

indicate that the cellulose fibers serve as both a chemical contributor and a physical bridge, leading to the successful healing of surface cracks.

### 3.2. Internal healing

#### 3.2.1. Induced cracks

Following three days of initial water curing, three specimens from each mixture were evaluated to determine their respective average breaking loads, as illustrated in Figure 11. The experimental results identify M1 as having the highest mechanical strength, exhibiting a peak breaking load of 12.17 kN, while the M5 mixture exhibited the lowest capacity at 8.26 kN. To induce internal cracks for the subsequent healing analysis, a load threshold of 90% of the breaking load was established for each specific mixture. The corresponding forces applied were 8.62, 10.95, 10.46, and 7.43 kN in M0, M1, M2, and M5, respectively,

as shown in Figure 11. By tailoring the induced stress to the individual capacity of each mixture, the study ensures that the internal damage is representative of the structural limits of the material, allowing for a rigorous assessment of the cellulose-facilitated recovery process.

Visual confirmation of the induced internal architecture is presented in Figure 12, where the transition from the original state to the fractured state is evident. While the 'before' state primarily features distributed entrained air voids, the 'after' state clearly displays the propagation of distinct internal crack networks resulting from the applied 90% breaking load. The application of the calibrated loads resulted in the formation of complex micro-crack geometries, which were monitored at 0, 3, 7, 14, and 28 days to observe the healing progression (Figure 13). This methodology facilitated the clear distinction between the preexisting pore structure and the newly induced cracks. By

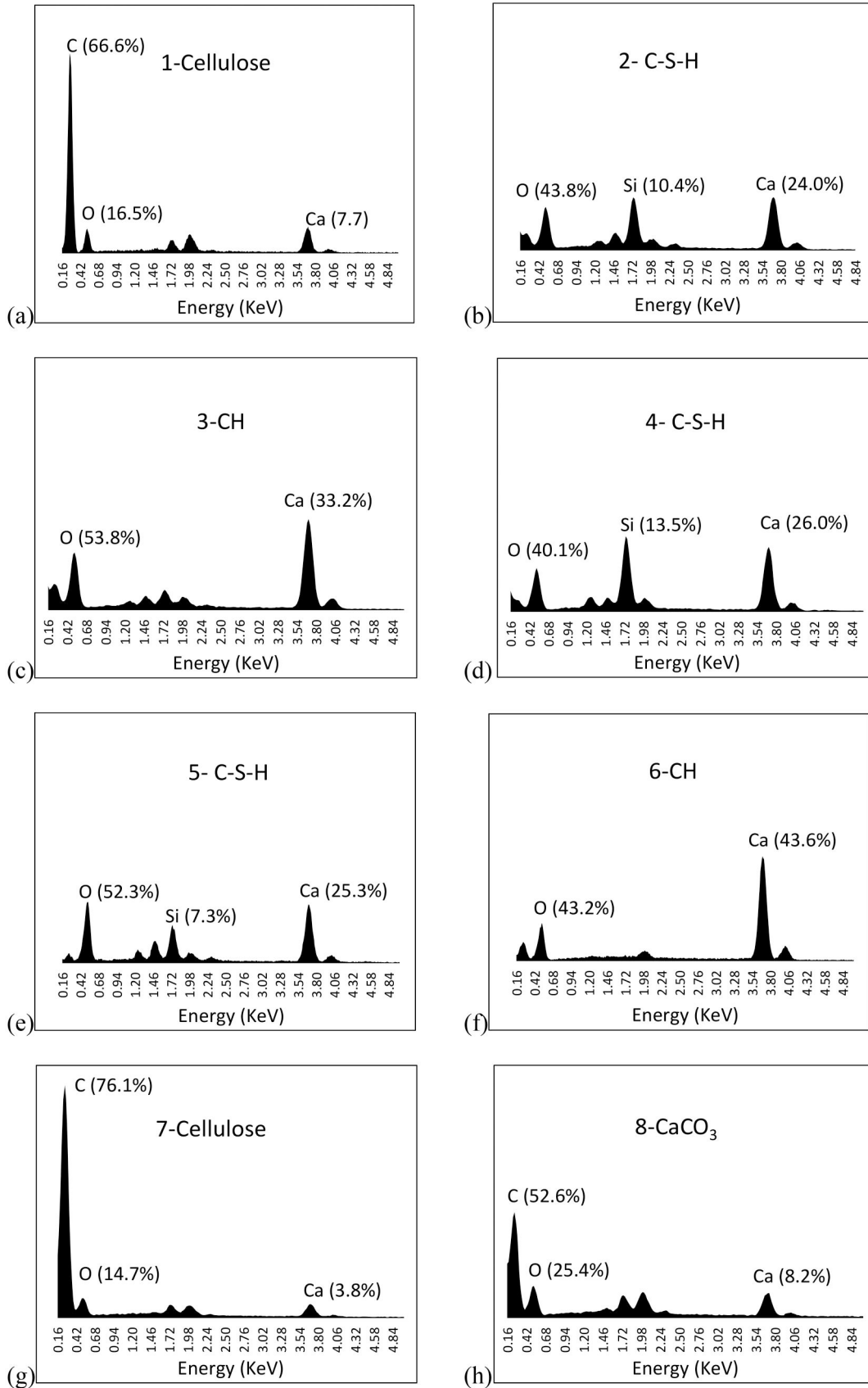


Figure 10. EDS spectra with atomic weight percentages of the compounds identified around cellulose in the cracks in (a-c) P1, (d-f) P2 and (g, h) in P5.

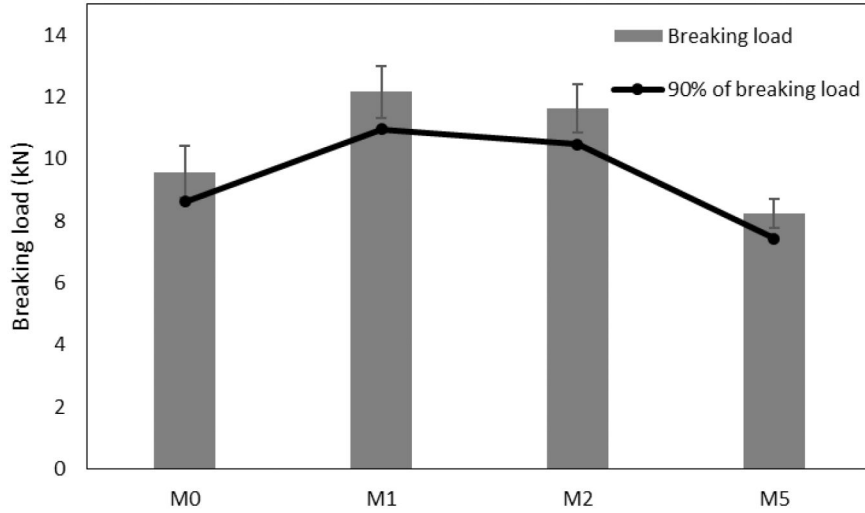


Figure 11. Breaking loads of mortar samples.

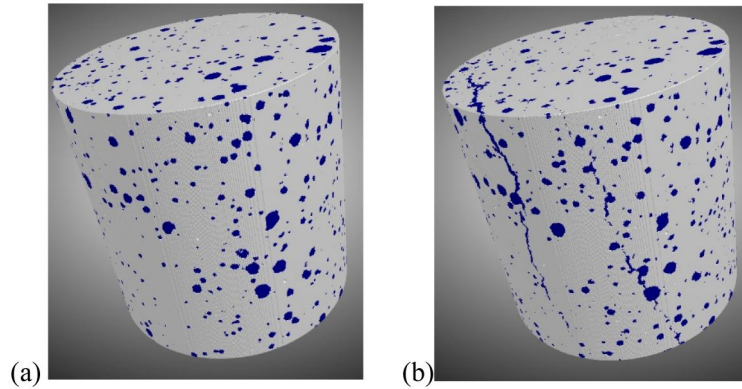


Figure 12. Reconstructed VOI (volume of interest) (a) before cracking and (b) after cracking.

isolating the crack-specific volume of interest (VOI), the subsequent sections provide a detailed morphometric analysis. Specifically, the variation in pore volume, changes in aspect ratio, and shifts in sphericity are analyzed to determine the efficacy of the recycled textile cellulose in bridging and sealing the internal structural damage over the 28-day curing timeframe.

### 3.2.2. Pore volume

Before the induction of internal damage, the initial porosity was found to be influenced by the cellulose replacement level, as presented in Figure 14a. Porosity values were determined to be 6.10%, 5.23%, 5.60%, and 6.78% for M0, M1, M2, and M5, respectively, with M1 exhibiting the most refined matrix, whereas M5 gave the highest porosity. Upon inducing cracks at 3 days, a sharp increase in total porosity was recorded across all specimens. However, throughout the 28-day healing period, the porosity values of all the samples reduced gradually, as shown in Figure 14b. Initial observations between 0 and 3 days post-loading showed that the M0 control achieved the most rapid reduction in porosity, likely due to residual free water from the initial water curing phase. However, as curing progressed beyond 3 days, the healing rate of the control slowed considerably compared to the cellulose

mixtures, suggesting that cellulose effectively facilitates sustained hydration through moisture retention.

The internal healing efficiency was quantified based on the porosity reduction of the samples over the 28-day curing interval, as presented in Figure 15. The results demonstrate a significant performance advantage in the cellulose-modified specimens, all of which exceeded the 11.8% efficiency observed in the control group. Most notably, the M2 mixture demonstrated the maximum internal healing efficiency, reaching a peak value of 22.1%. This superior performance aligns with the optimal dosage observed in the surface healing tests, confirming that a 2% cellulose replacement provides the most effective internal curing environment. While M1 and M5 also demonstrated improved recovery over the control, with efficiencies of 15.5% and 12.2%, respectively, their comparative underperformance relative to M2 highlights a critical dosage threshold. Beyond this 2% replacement level, fiber clustering (as observed in SEM analysis) likely restricts the effective sealing of the voids.

To further characterize the microstructural refinement, the void volume distribution was analyzed at all curing stages, as illustrated in Figure 16. In this analysis, ‘frequency’ refers to the numerical count of individual, discrete void objects identified within the 3D volume. Notably, the distribution of voids smaller than  $0.005\text{mm}^3$

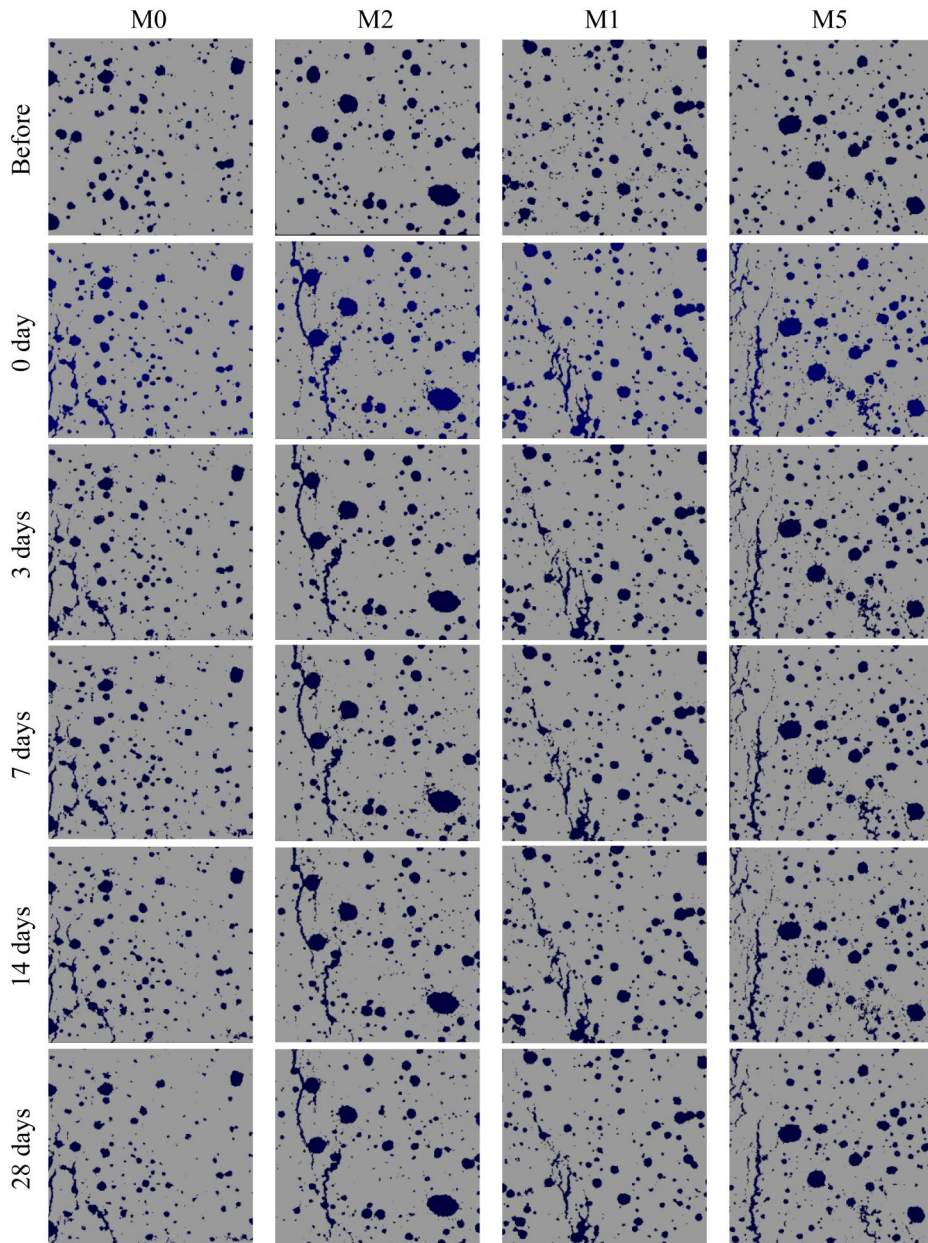


Figure 13. Crack healing of mortar samples over time.

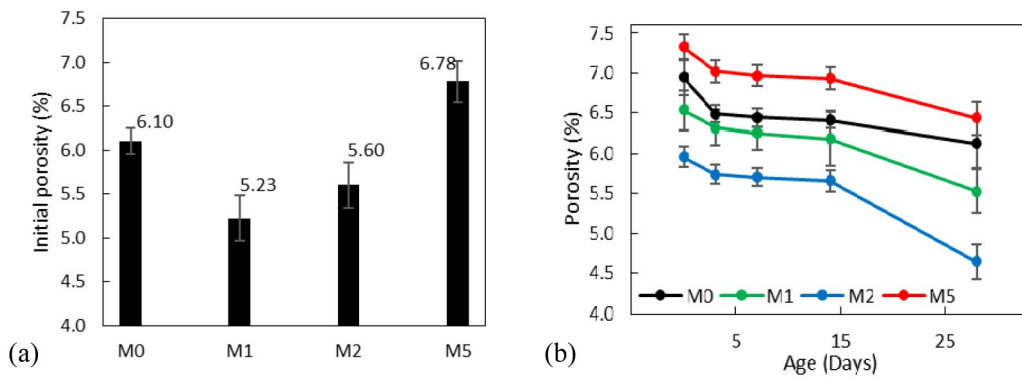


Figure 14. Measured porosity: (a) initial porosity, (b) porosity variation during healing.

underwent significant fluctuations during the experimental cycle, while the pre-damaged state exhibited the lowest frequency of these small-scale voids, their number increased sharply immediately following the induction of

damage. During the subsequent healing period, this frequency gradually declined in all specimens, though the reduction was more pronounced in the cellulose composites compared to the control. Specifically, in the M1 and

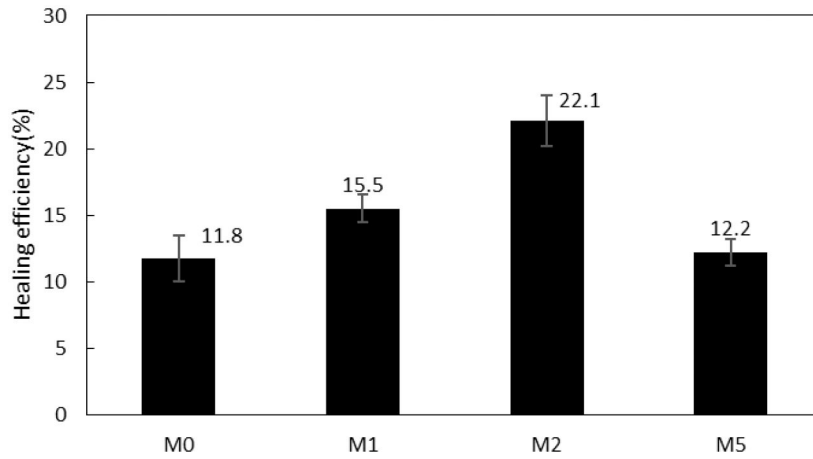


Figure 15. Healing efficiency during the 28-day healing period.

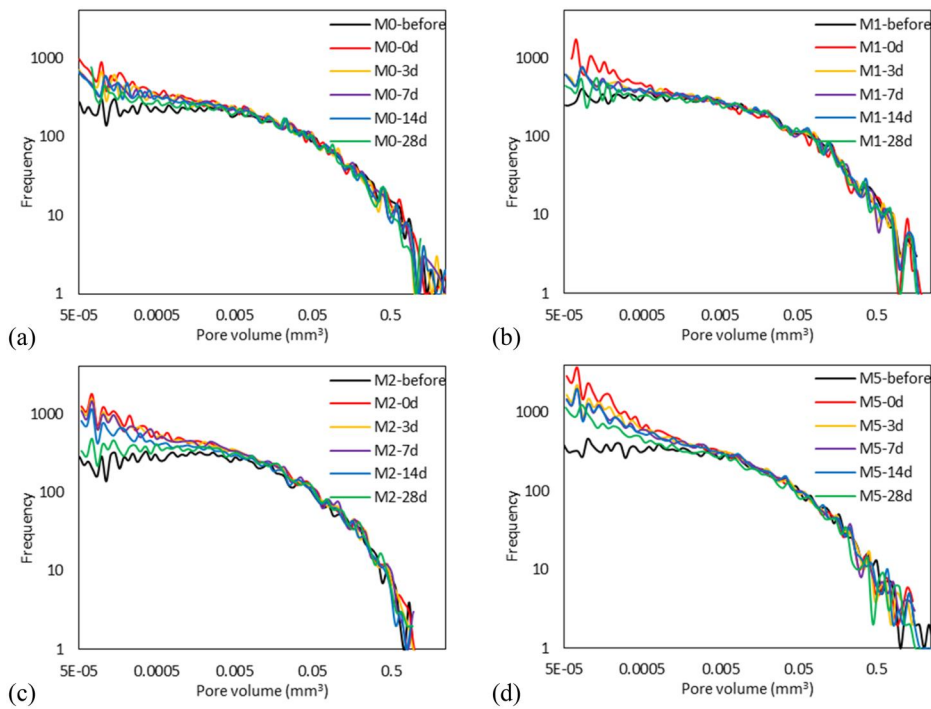


Figure 16. Volume distribution of voids at all stages in (a) M0, (b) M1, (c) M2, and (d) M5.

M2 specimens, the frequency of these voids returned to much closer to the initial pre-damaged baseline, whereas M0 and M5 maintained a higher residual count. This transition from larger crack volumes to finer pore structures, particularly the recovery of the small-scale matrix architecture, provides quantitative evidence of successful internal sealing.

### 3.2.3. Sphericity and aspect ratio

The geometric transformation of internal voids was quantified using two primary metrics: sphericity and aspect ratio. Sphericity values range from 0 to 1 [29], where voids with sphericity between 0.6 and 1 are classified as pores [34], while those falling between 0 and 0.6 are identified as cracks. Similarly, the aspect ratio was also utilized to distinguish spherical pores from elongated micro-cracks. Following established criteria for cement-based materials, voids with an aspect ratio between 1 and

6 were classified as pores [31], whereas those with a ratio greater than 6 are characterized as elongated features, which include macro and micro cracks.

Using these classification criteria, all detected voids were separated into two categories based on their sphericity and aspect ratio values. The frequency distribution of these classified voids before and after the 28-day healing period is illustrated in Figure 17 (based on sphericity) and Figure 18 (based on aspect ratio). The counts of both pores and cracks decreased significantly across all mixtures after the 28-day curing period. While the control (M0) exhibited limited healing, the cellulose-modified composites demonstrated a significantly more pronounced reduction in internal voids. Notably, the M2 mixture demonstrated the highest efficiency, achieving a reduction of 61.2% for cracks and 59.2% for pores, based on the sphericity variation of the voids. A similar trend is observed with the variation of the aspect ratio values. This suggests

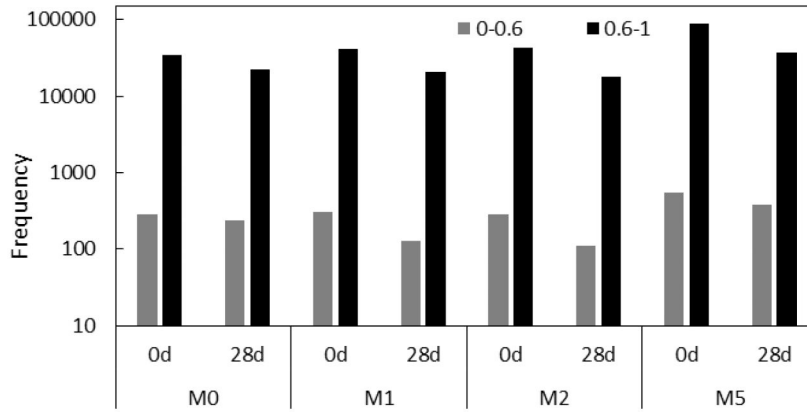


Figure 17. Frequency distribution of voids based on sphericity before and after the 28-day healing period.

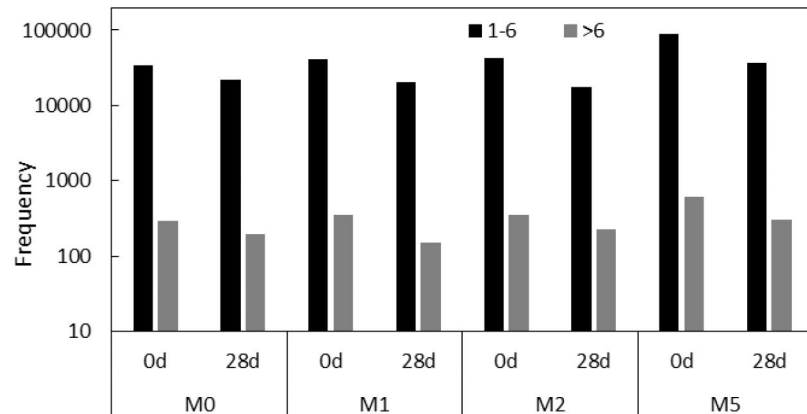


Figure 18. Frequency distribution of voids based on aspect ratio before and after the 28-day healing period.

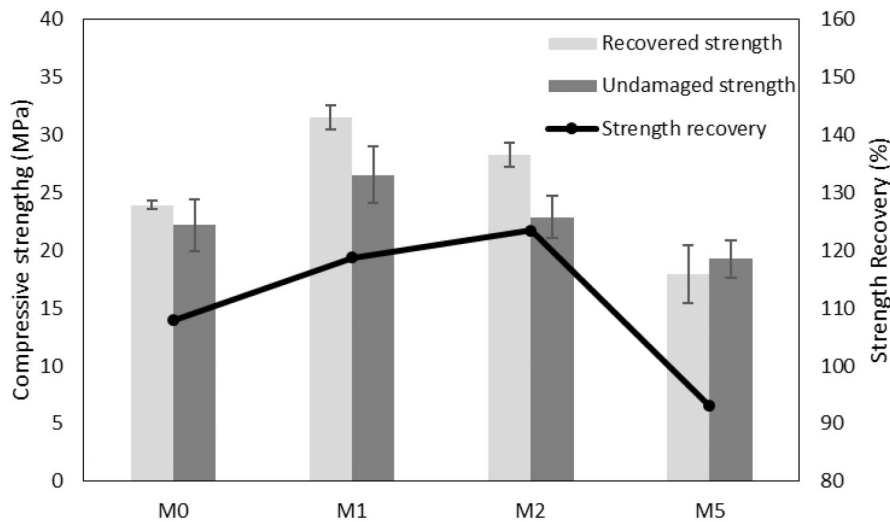


Figure 19. Mechanical strength recovery of the samples.

that the internal curing effect of the 2% cellulose dosage is uniquely effective at facilitating mineral precipitation even in highly elongated crack geometries.

### 3.3. Mechanical strength recovery

The mechanical performance of the mortar specimens following the 28-day healing period is illustrated in Figure 19, which compares the recovered compressive strength of the healed samples against the strength of undamaged

specimens at the same age. A critical observation from the experimental data is that for most mixtures, the recovered strength surpassed the strength of age-matched virgin specimens. This phenomenon suggests that the moist curing conditions, combined with enhanced moisture penetration through the induced crack network, potentially densified the overall matrix to a greater degree than the original state. While the dense matrix of undamaged specimens restricts water penetration to surface regions, the microcracks serve as preferential pathways for deeper

moisture ingress, enabling water to reach unhydrated cementitious particles within the specimen core [35,36]. This facilitates the hydration of unreacted cement particles that would otherwise remain inactive [37], with the resulting precipitation of hydration products not only sealing the cracks but further densifying the internal microstructure, leading to strength gains exceeding those of age-matched virgin specimens. However, it is important to note that this recovery exceeding 100% does not necessarily indicate complete crack sealing. Rather, it is attributed to a combination of the factors discussed, which may enhance the overall load-bearing capacity of the specimen independently of crack closure extent.

In terms of absolute performance, the M1 mixture exhibited the highest compressive strength in both the healed and undamaged states, reaching 31.5 and 26.6 MPa, respectively. M1 therefore, represents the optimum dosage in terms of undamaged matrix strength. Despite the superior strength values of M1, the M2 mixture achieved the highest strength recovery ratio, peaking at 123.5%. M2 therefore, represents the optimum dosage specifically in terms of healing-assisted mechanical recovery. This indicates that while M1 provides the most robust structural matrix, the 2% cellulose replacement in M2 offers the optimal environment for autogenous healing and mechanical restoration.

Conversely, the M5 mixture showed a notable decline in performance, exhibiting the lowest compressive strength values and a recovery ratio that fell below 100%, reaching roughly 93%. This underperformance correlates with earlier microstructural observations of fiber agglomeration and increased initial porosity in high-dosage cellulose samples. Furthermore, it is observed that while the control (M0) demonstrated a recovery ratio above 100%, its absolute strength remained significantly lower than the M1 and M2 composites. Collectively, these results illustrate that an optimal cellulose dosage can significantly augment the mechanical resilience of mortar, allowing for the effective recovery and, in some cases, the enhancement of structural capacity following significant internal damage.

## 4. Discussion

The experimental findings demonstrate that the integration of recycled textile-derived cellulose significantly enhances the self-healing capacity of cementitious composites. This enhancement is evident in both macroscopic surface crack closure and internal volumetric refinement. The synergistic interaction between the intrinsic autogenous healing of the cement matrix and the unique properties of cellulose fibers acting as internal moisture reservoirs and structural bridges provides a robust mechanism for sustained material recovery.

### 4.1. Mechanism of cellulose-enhanced healing

The superior performance of cellulose-modified specimens (P2 and M2) can be attributed to the internal curing effect driven by the moisture gradient within the

matrix. Cellulose fibers are characterized by a porous, hydrophilic structure that allows them to absorb and retain significant amounts of water during the initial mixing stage, with some studies reporting retention capacities as high as 85–947% of the weight of the fibers [14,18], depending on the cellulose morphology and degree of fibrillation. As the cement matrix undergoes self-desiccation or crack formation, these fibers slowly release the stored water into the surrounding non-hydrated cement particles, driven by the relative humidity difference, thereby maintaining a favorable environment for continued hydration reactions [15,38].

The released moisture facilitates continuous hydration, leading to the formation of additional hydration products, primarily calcium silicate hydrate (C-S-H) and calcium hydroxide (CH). At the fiber-matrix interface, the hydroxyl groups on cellulose chains are proposed, consistent with prior literature [16,39,40], to couple with calcium ions in the pore solution, forming covalent bonds that densify the interfacial zone and promote localized C-S-H nucleation, a mechanistic interpretation supported by literature rather than directly demonstrated by the experimental techniques employed in this study. As evidenced in Section 3.1.2, the inclusion of cellulose fibers also promotes localized precipitation of  $\text{CaCO}_3$  along the fiber-crack interface. Building on these interfacial interactions, the three-dimensional network of cellulose fibers distributed throughout the matrix, formed by the interconnected arrangement of hydrophilic fibers embedded within the cement paste during mixing, is further proposed to create a ‘short-circuit diffusion’ pathway [39,40], facilitating the migration of water molecules and  $\text{Ca}^{2+}$  ions from the matrix interior to the crack surface. This proposed transport mechanism, while consistent with the present EDS observations of healing product distribution, is inferred from prior literature rather than directly measured in this study. Together, these chemical and transport contributions drive the progressive deposition of C-S-H, CH, and  $\text{CaCO}_3$  within the crack void, ultimately sealing the crack interior. This mineralized seal effectively bridges the crack voids, as highlighted in the SEM observations, a phenomenon consistent with findings by Ataabadi et al. who noted that friction and bending at crack surfaces can further stimulate crystal growth perpendicular to the crack walls [21].

Beyond these chemical contributions, cellulose fibers provide a physical bridging effect. The fibrous nature of the material allows it to span micro-crack voids, acting as a structural skeleton that stabilizes the crack interior. By restricting the crack width during the plastic phase, cellulose fibers keep the crack dimensions within the healable range (typically  $< 150 \mu\text{m}$ ), which is a critical prerequisite for effective autogenous healing [14,37]. Furthermore, surface analysis suggests that the presence of cellulose may facilitate the nucleation of hydration products, providing sites for crystals to anchor and grow across the damage interface due to the presence of additional moisture in cellulose (Figure 20). This high specific surface area of the fibers effectively lowers the energy barrier for

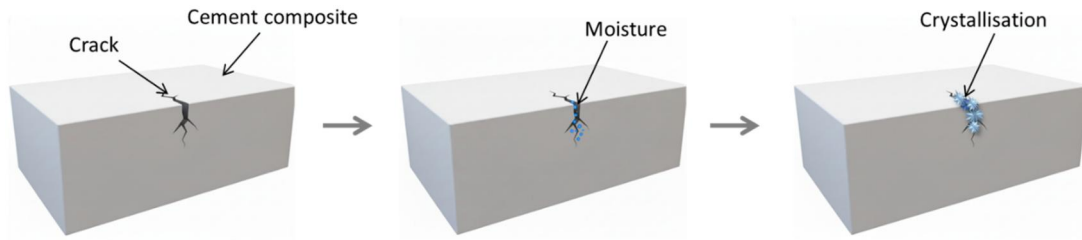


Figure 20. Healing mechanism with the presence of moisture (adapted from [14]).

precipitation, allowing hydration products to accumulate at a high density around the fiber network [16,41]. However, this is presented as a literature-supported interpretation rather than a directly demonstrated mechanism.

The experimental data suggest that the success of cellulose-enhanced healing is highly dependent on achieving a uniform fiber distribution, with 2% replacement emerging as the most effective dosage. This balanced state allows for the most efficient development of hydration products within the crack planes. When the dosage is increased to 5%, however, the fibers tend to cluster together, forming pockets of high porosity that actually weaken the sample and interfere with the uniform distribution of healing agents. Literature notes that excessive fiber content leads to agglomeration and entanglement, creating fiber pockets that introduce defects rather than reinforcement [39,42]. These agglomerations increase the volume of macro-pores and create weak interfacial transition zones (ITZ) that offset the benefits of internal curing [18,23].

The spatial evolution of internal damage and subsequent repair is visualized in Figure 21 through a differential volume analysis. The ‘Cracks created’ images were generated by subtracting the pre-damage (undamaged) voids VOI from the 0-day post-cracking scan, effectively isolating the new voids introduced by the 90% breaking load. Similarly, ‘Cracks healed’ were identified by subtracting the voids in the 28-day scan volume from those in the 0-day scan, revealing the regions where new hydration products or precipitates successfully filled the void space. This subtractive methodology aligns with protocols established in recent Micro-CT studies, which successfully utilized differential volume rendering to quantify the exact volume of healing products formed within internal fractures [30,43]. While both samples show a similar initial damage pattern, healing reveals the superior performance of the M2 sample. In M2, the healing products are not merely scattered but are densely concentrated along the primary crack planes. This indicates that the cellulose fibers acted as local moisture reservoirs, specifically targeting the high-aspect-ratio voids for precipitation.

While conventional mortar demonstrated a baseline internal healing efficiency of approximately 12% under humid conditions (based on porosity reduction), cellulose-modified samples achieved a superior internal healing rate of approximately 22%. Surface crack healing showed similar trends, with control specimens achieving 4.9% closure compared to 10.5% for the optimal 2% cellulose formulation. While these metrics derive from

complementary but distinct test configurations, the consistent superior performance of the 2% dosage across both series provides converging evidence for its designation as the experimental optimum. Although these figures represent a moderate degree of repair, they are consistent with autogenous mechanisms typical of high-humidity, non-saturated curing, where the lack of liquid water limits the transport of dissolved calcium ions necessary for calcite precipitation [44,45]. In this moisture-limited environment, the results show that cellulose serves to augment the natural healing response by functioning as an internal water reservoir. Due to their hydrophilic nature and high water retention capacity, cellulose fibers can effectively store and release moisture to unhydrated cement particles, thereby sustaining hydration reactions, even when external water is scarce [18]. Comparative studies indicate that healing efficiencies can jump from approximately 15% in humidity chambers to over 90% under full water immersion [45]. Therefore, under continuous immersion, the synergy between cellulose-mediated moisture transport and increased external water ingress would likely yield substantially greater healing by facilitating the extensive crystallization of calcium carbonate [19,36]. These findings highlight that 2% cellulose replacement achieves optimal balance between effective fiber dispersion and internal curing efficiency, establishing the mechanistic foundation for cellulose-enhanced autogenous healing in cementitious composites.

#### 4.2. Geometric refinement

The Micro-CT data indicate that cellulose-induced healing acts as a geometric filter, preferentially targeting structural defects compared to standard capillary pores. This process, termed geometric attenuation, transforms the void network from a system of interconnected fractures to one of isolated, smaller voids. Quantitatively, this is demonstrated by the specific reduction of features with low sphericity ( $<0.6$ ) and high aspect ratios ( $>6$ ). In the M2 sample, the 61.2% reduction in these elongated features illustrates the efficacy of the cellulose reinforcement.

Unlike passive fillers, cellulose fibers actively reinforce the interior of the crack through a scaffolding mechanism. The fiber distributing throughout the void space and linking individual healing crystals into a dense, consolidated network rather than passively filling the crack [16]. Furthermore, internal curing fuels the growth of hydration products directly within the crack path [38,46]. This localized mineralization segments the plate-like cracks into rod-like or spherical voids, effectively

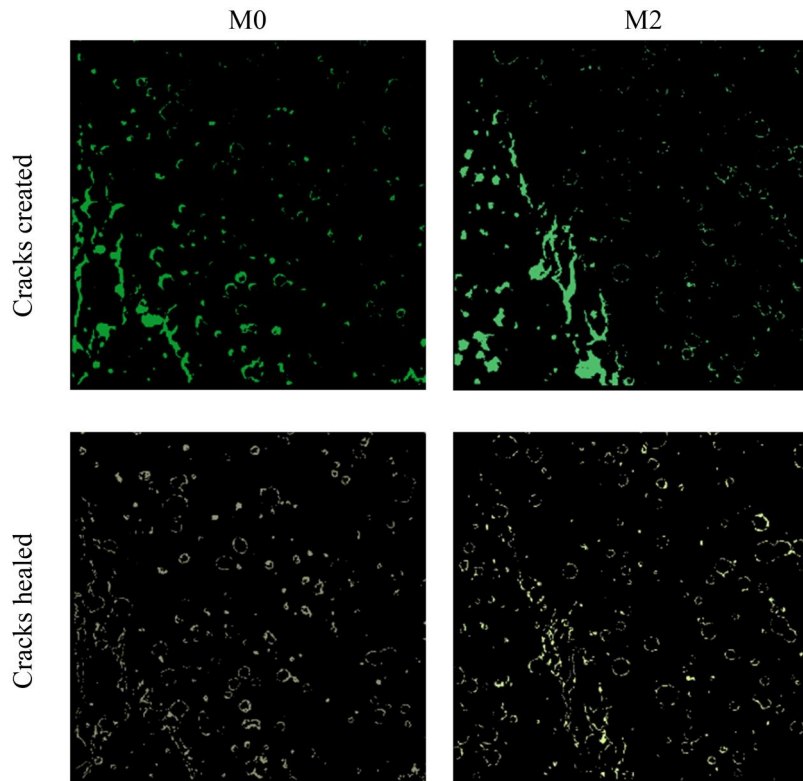


Figure 21. Spatial evolution of the created cracks (light green) and healed cracks (yellow) in M0 and M2, illustrating the contrasting healing response between the control and cellulose-modified systems.

increasing the structure model index (SMI) of the void space [28]. The result is a refined microstructure where continuous pathways for aggressive agents are severed, effectively transforming the interconnected fracture network into a system of discontinuous, isolated voids [47].

#### 4.3. Implications for structural durability

The transition from a fractured state to a healed, and in some cases self-strengthened, state is of paramount importance for the lifespan of concrete infrastructure. Experimental evidence indicates that the mechanical recovery of cellulose-reinforced composites often exceeds the strength of undamaged control specimens, a phenomenon quantified by compressive strength recovery values greater than 100% [21,35]. This self-strengthening suggests that the later-age hydration promoted by cellulose densifies the matrix beyond its original virgin state [16,36]. Unlike standard autogenous healing, which is limited by the availability of water, cellulose fibers function as internal water reservoirs; they release stored moisture to hydrate unreacted cement particles within the matrix, thereby mitigating self-desiccation and promoting the formation of additional C-S-H gels [18,38].

This internal curing is particularly vital for durability in aggressive environments. By autogenously sealing cracks as they form, the material has the potential to limit the ingress of harmful agents. Although specific durability metrics were not quantified in the current experimental scope, the partial crack sealing carries implications for the long-term resilience of the material. Previous research has observed that the physical blocking of cracks by healing

products, alongside global matrix densification, drastically reduces the transport of liquids and gases through the concrete [37,48]. Because the penetration of aggressive agents is highly correlated with crack opening [41], the autogenous repairing observed in this study is expected to impede chloride permeation and inhibit corrosion [36,37]. Additionally, in sulfate-bearing conditions, autonomous crack repair mitigates sulfate attack on the concrete matrix, preventing the expansive deterioration that would otherwise create pathways for further aggressive agent ingress [37,49]. Research on Ultra-High-Performance Concrete (UHPC) modified with cellulose nanofibers has demonstrated that such composites can achieve 100% crack sealing efficiency, even when exposed to geothermal waters rich in aggressive ions, significantly outperforming control samples [19]. The presence of cellulose not only restricts the crack width during the plastic phase, reducing water permeability coefficients by up to 42% [14], but also refines the pore structure through the precipitation of healing products like calcite and C-S-H [21,44]. However, it is important to acknowledge that the present study does not include direct durability-related measurements such as permeability, sorptivity, water absorption, or chloride transport testing. Moreover, while micro-CT analysis confirms partial void reduction, the connectivity of the remaining crack and pore network, which governs liquid penetration and chemical ingress was not directly characterized. As such, the extent to which the observed healing response can prevent aggressive agent ingress, particularly relative to uncracked specimens, remains to be established through dedicated transport-based investigations, which are recommended as

a priority for future work. Consequently, this technology shows potential to contribute to a shift in the maintenance paradigm from reactive repair to active self-maintenance, offering substantial reductions in life-cycle costs and environmental impact [4,37].

The experimental results provide guidance for dosage selection based on application requirements. While M1 demonstrated the highest absolute strength, M2 emerged as the most efficient configuration for post-damage strength recovery, achieving the highest recovery ratio relative to its undamaged state. This distinction highlights that the optimum cellulose content is not a singular value but depends on the specific performance requirements of the application. Consequently, a 1% replacement is most suitable for general structural applications where load-bearing capacity is paramount. However, the selection shifts in favor of the 2% dosage for durability-critical infrastructure, such as marine or water-retaining structures. In these environments, crack-width control and watertightness are more critical. In such cases, the ability of M2 to more aggressively seal the pore network and restore mechanical integrity through internal curing offers a more reliable defence against the ingress of aggressive agents and subsequent reinforcement corrosion. Therefore, M2 represents the ideal equilibrium where chemical benefits are leveraged to specifically to optimize the long-term resilience of the structure.

## 5. Conclusions

The experimental investigation establishes that recycled textile-derived cellulose enhances self-healing in cementitious composites through a dual mechanism that combines cellulose-mediated internal curing with autogenous cement hydration. Although surface and internal healing were assessed through different specimen types and crack induction methods, 2% cellulose incorporation consistently demonstrated superior healing efficiency across all evaluated metrics, surface crack closure, internal void reduction, and strength recovery, providing convergent experimental evidence for identification as the optimum dosage within the adopted testing program. The following conclusions are drawn from this study:

1. Recycled textile-derived cellulose functions as an effective self-healing agent by promoting continued autogenous hydration, with execution efficiency influenced by initial crack width, curing duration, and cellulose dosage.
2. Optimal self-healing performance within the adopted experimental conditions is consistently achieved at 2% cellulose replacement, delivering 10.46% surface healing, 22.1% internal healing efficiency, and 123.5% mechanical strength recovery.
3. Surface healing was most rapid during 3–7 days, while internal healing peaked during 14–28 days.
4. Advanced geometric analysis using void aspect ratio and sphericity parameters confirms successful healing, demonstrating systematic refinement of the internal microstructure over time.

5. Microstructural characterization identified C–S–H, CH, and CaCO<sub>3</sub> as healing products, with cellulose fibers providing physical micro-bridging across void spaces.
6. Although absolute healing values remain moderate, consistent improvement relative to the control, is evident across all measured metrics. These values reflect the experimental conditions adopted, particularly the use of humidity curing rather than full immersion and the limited observation period.

## Acknowledgements

The facilities and scientific and technical assistance of the RMIT Microscopy & Microanalysis Facility (RMMF), a linked laboratory of Microscopy Australia enabled by NCRIS, are also acknowledged, with special appreciation to Dr. Chaitali Dekiwadia for technical assistance in micro-CT scanning. The authors also thank Vital Chemical Pty Ltd for providing the recycled cellulose used in the study.

## Author contributions

CRedit: **Chamini Liyanage**: Conceptualization, Data curation, Formal analysis, Investigation, Methodology, Writing – original draft; **Chamila Gunasekara**: Conceptualization, Funding acquisition, Resources, Supervision, Writing – review & editing; **Magdalena Rajczakowska**: Methodology, Supervision, Writing – review & editing; **David W. Law**: Supervision, Writing – review & editing; **Sujeeva Setunge**: Supervision, Writing – review & editing.

## Disclosure statement

The authors report there are no competing interests to declare.

## Funding

The authors acknowledge funding from the Australian Research Council (TREMS and DE230101221).

## References

- [1] Mengel L, Krauss H-W, Lowke D. Water transport through cracks in plain and reinforced concrete – influencing factors and open questions. *Constr Build Mater.* 2020;254:118990. doi: [10.1016/j.conbuildmat.2020.118990](https://doi.org/10.1016/j.conbuildmat.2020.118990).
- [2] Sonali Sri Durga C, Ruben N. Assessment of various self healing materials to enhance the durability of concrete structures. *Ann Chim Sci Mat.* 2019;43(2):75–79.
- [3] Dong S, Zhang W, Wang X, et al. New-generation pavement empowered by smart and multifunctional concretes: a review. *Constr Build Mater.* 2023;402:132980. doi: [10.1016/j.conbuildmat.2023.132980](https://doi.org/10.1016/j.conbuildmat.2023.132980).
- [4] Li VC, Herbert E. Robust self-healing concrete for sustainable infrastructure. *ACT.* 2012;10(6):207–218. doi: [10.3151/jact.10.207](https://doi.org/10.3151/jact.10.207).
- [5] Schlangen E, Sangadji S. Addressing infrastructure durability and sustainability by self healing mechanisms -

- recent advances in self healing concrete and asphalt. *Procedia Eng.* 2013;54:39–57. doi: [10.1016/j.proeng.2013.03.005](https://doi.org/10.1016/j.proeng.2013.03.005).
- [6] Park B, Choi YC. Prediction of self-healing potential of cementitious materials incorporating crystalline admixture by isothermal calorimetry. *Int J Concr Struct Mater.* 2019;13(1):36. doi: [10.1186/s40069-019-0349-9](https://doi.org/10.1186/s40069-019-0349-9).
- [7] Liu JL, Li Y, Jin CY, et al. Preparation and mechanism analysis of nanocrystalline cellulose-tricalcium silicate paste composite with high electromagnetic transmission performance. *Cement Concrete Comp.* 2023;143:105233 doi: [10.1016/j.cemconcomp.2023.105233](https://doi.org/10.1016/j.cemconcomp.2023.105233).
- [8] Ghahari S, Assi LN, Alsalmán A, et al. Fracture properties evaluation of cellulose nanocrystals cement paste. *Materials.* 2020;13(11):2507. doi: [10.3390/ma13112507](https://doi.org/10.3390/ma13112507).
- [9] Cao Y, Zavaterra P, Youngblood J, et al. The influence of cellulose nanocrystal additions on the performance of cement paste. *Cem Concr Compos.* 2015;56:73–83. doi: [10.1016/j.cemconcomp.2014.11.008](https://doi.org/10.1016/j.cemconcomp.2014.11.008).
- [10] Bentschikou M, Guidoum A, Scrivener K, et al. Effect of recycled cellulose fibres on the properties of lightweight cement composite matrix. *Constr Build Mater.* 2012;34:451–456. doi: [10.1016/j.conbuildmat.2012.02.097](https://doi.org/10.1016/j.conbuildmat.2012.02.097).
- [11] Peña-Pichardo P, Martínez-Barrera G, Martínez-López M, et al. Recovery of cotton fibers from waste blue-jeans and its use in polyester concrete. *Constr Build Mater.* 2018;177:409–416. doi: [10.1016/j.conbuildmat.2018.05.137](https://doi.org/10.1016/j.conbuildmat.2018.05.137).
- [12] Zhang X, Lei C, Li Z, et al. Effect of cellulose nanofibrils on the physical properties and frost resistance of pervious concrete. *Materials (Basel).* 2022;15(22):7906. doi: [10.3390/ma15227906](https://doi.org/10.3390/ma15227906).
- [13] Zhang Z, Angst U. Microstructure and moisture transport in carbonated cement-based materials incorporating cellulose nanofibrils. *Cem Concr Res.* 2022;162:106990. doi: [10.1016/j.cemconres.2022.106990](https://doi.org/10.1016/j.cemconres.2022.106990).
- [14] Singh H, Gupta R. Influence of cellulose fiber addition on self-healing and water permeability of concrete. *Case Stud Constr Mater.* 2020;12:e00324. doi: [10.1016/j.cscm.2019.e00324](https://doi.org/10.1016/j.cscm.2019.e00324).
- [15] Wu H, Shen A, Cheng Q, et al. A review of recent developments in application of plant fibers as reinforcements in concrete. *J Cleaner Prod.* 2023;419:138265. doi: [10.1016/j.jclepro.2023.138265](https://doi.org/10.1016/j.jclepro.2023.138265).
- [16] Zhang F, Pang K, Li J, et al. Effect of micro-cellulose fiber on the mechanical, shrinkage properties and ballistic impact resistance of high-performance cement composites. *Constr Build Mater.* 2025;463:139963. doi: [10.1016/j.conbuildmat.2025.139963](https://doi.org/10.1016/j.conbuildmat.2025.139963).
- [17] Ardanuy M, Claramunt J, Toledo RD. Cellulosic fiber reinforced cement-based composites: a review of recent research. *Constr Build Mater.* 2015;79:115–128. doi: [10.1016/j.conbuildmat.2015.01.035](https://doi.org/10.1016/j.conbuildmat.2015.01.035).
- [18] Jaberizadeh MM, Danoglidis PA, Shah SP, et al. Eco-efficient cementitious composites using waste cellulose fibers: effects on autogenous shrinkage, strength and energy absorption capacity. *Constr Build Mater.* 2023;408:133504. doi: [10.1016/j.conbuildmat.2023.133504](https://doi.org/10.1016/j.conbuildmat.2023.133504).
- [19] Cuenca E, Mezzena A, Ferrara L. Synergy between crystalline admixtures and nano-constituents in enhancing autogenous healing capacity of cementitious composites under cracking and healing cycles in aggressive waters. *Constr Build Mater.* 2021;266:121447. doi: [10.1016/j.conbuildmat.2020.121447](https://doi.org/10.1016/j.conbuildmat.2020.121447).
- [20] Singh H, Gupta R. Cellulose fiber as bacteria-carrier in mortar: self-healing quantification using UPV. *J Build Eng.* 2020;28:101090. doi: [10.1016/j.job.2019.101090](https://doi.org/10.1016/j.job.2019.101090).
- [21] Sanaei Ataabadi H, Liu Y, Zeng J-J, et al. Unveiling the impact of absorbent polymers on self-healing efficiency of sludge-derived capsules in cementitious composites. *Constr Build Mater.* 2024;451:138803. doi: [10.1016/j.conbuildmat.2024.138803](https://doi.org/10.1016/j.conbuildmat.2024.138803).
- [22] Savastano H, Jr. Warden PG, Coutts RSP. Mechanically pulped sisal as reinforcement in cementitious matrices. *Cement Concrete Comp.* 2003;25(3):311–319. doi: [10.1016/S0958-9465\(02\)00055-0](https://doi.org/10.1016/S0958-9465(02)00055-0).
- [23] Liyanage C, Gunasekara C, Law DW, et al. Textile-cellulose as a secondary modifier in graphene and SCM-based cement paste. *J Build Eng.* 2025;113:114169. doi: [10.1016/j.job.2025.114169](https://doi.org/10.1016/j.job.2025.114169).
- [24] Standards Australia. General purpose and blended cements (AS 3972). Sydney, Australia: Standards Australia; 2010.
- [25] ASTM International. Standard specification for concrete aggregates (ASTM C33/C33M). 100 Barr Harbor Drive, PO Box C700, West Conshohocken, PA 19428-2959, United States.: ASTM International; 2024.
- [26] ASTM International. Standard test method for compressive strength of hydraulic cement mortars (using 50 mm [2 in.] cube specimens) (ASTM C109/C109M). West Conshohocken, PA: ASTM International; 2024.
- [27] ASTM international. Standard practice for mechanical mixing of hydraulic cement pastes and mortars of plastic consistency (ASTM C305). West Conshohocken, PA: ASTM International; 2020.
- [28] Sidiq A, Setunge S, Gravina RJ, et al. Self-repairing cement mortars with microcapsules: a microstructural evaluation approach. *Constr Build Mater.* 2020;232:117239. doi: [10.1016/j.conbuildmat.2019.117239](https://doi.org/10.1016/j.conbuildmat.2019.117239).
- [29] Sidiq A, Gravina RJ, Setunge S, et al. Microstructural analysis of healing efficiency in highly durable concrete. *Constr Build Mater.* 2019;215:969–983. doi: [10.1016/j.conbuildmat.2019.04.233](https://doi.org/10.1016/j.conbuildmat.2019.04.233).
- [30] Suleiman AR, Nelson AJ, Nehdi ML. Visualization and quantification of crack self-healing in cement-based materials incorporating different minerals. *Cem Concr Compos.* 2019;103:49–58. doi: [10.1016/j.cemconcomp.2019.04.026](https://doi.org/10.1016/j.cemconcomp.2019.04.026).
- [31] Yu F, Sun D, Hu M, et al. Study on the pores characteristics and permeability simulation of pervious concrete based on 2D/3D CT images. *Constr Build Mater.* 2019;200:687–702. doi: [10.1016/j.conbuildmat.2018.12.135](https://doi.org/10.1016/j.conbuildmat.2018.12.135).
- [32] Herath C, Gunasekara C, Law DW, et al. Long term mechanical performance of nano-engineered high volume fly ash concrete. *J Build Eng.* 2021;43:103168. doi: [10.1016/j.job.2021.103168](https://doi.org/10.1016/j.job.2021.103168).
- [33] Li P, Li W, Wang K, et al. Hydration and microstructure of cement paste mixed with seawater – an advanced investigation by SEM-EDS method. *Constr Build Mater.* 2023;392:131925. (doi: [10.1016/j.conbuildmat.2023.131925](https://doi.org/10.1016/j.conbuildmat.2023.131925)).
- [34] Du Plessis A, Boshoff WP. A review of X-ray computed tomography of concrete and asphalt construction materials. *Constr Build Mater.* 2019;199:637–651. doi: [10.1016/j.conbuildmat.2018.12.049](https://doi.org/10.1016/j.conbuildmat.2018.12.049).
- [35] Rajczakowska M, Tole I, Hedlund H, et al. Autogenous self-healing of low embodied energy cementitious materials: effect of multi-component binder and crack geometry. *Constr Build Mater.* 2023;376:130994. doi: [10.1016/j.conbuildmat.2023.130994](https://doi.org/10.1016/j.conbuildmat.2023.130994).
- [36] Luan C, Yuan L, Wang J, et al. Uncovering the mechanism of the role of fly ash in the self-healing ability of mortar with different curing ages. *Materials.* 2023;16(9):3453. doi: [10.3390/ma16093453](https://doi.org/10.3390/ma16093453).
- [37] Amoorezaei K, Ghanbari-Ghazijahani T. A comprehensive review: self-healing methods and cementitious composites. *Structures.* 2025;72:108038. doi: [10.1016/j.istruc.2024.108038](https://doi.org/10.1016/j.istruc.2024.108038).
- [38] Rhee JH, Gwon S, Sim S, et al. Mitigating self-desiccation of cement composites via cellulose microfibrils:

- evidence of the microscopic behavior. *Constr Build Mater.* 2023;399:132585. doi: [10.1016/j.conbuildmat.2023.132585](https://doi.org/10.1016/j.conbuildmat.2023.132585)
- [39] Xuan MY, Wang XY. Multi-technique investigation regarding the impact of cellulose nanofibers on ultra-high-performance concrete at the macroscopic and microscopic levels. *Constr Build Mater.* 2022;327:126936. doi: [10.1016/j.conbuildmat.2022.126936](https://doi.org/10.1016/j.conbuildmat.2022.126936).
- [40] Xing X, Zhong G, Wu Z, et al. Self-healing mechanism of deposited carbonates in cement cracks under CO<sub>2</sub> storage well conditions [original research]. *Front Mater.* 2022;9:1013545. doi: [10.3389/fmats.2022.1013545](https://doi.org/10.3389/fmats.2022.1013545).
- [41] Cuenca E, Postolachi V, Ferrara L. Cellulose nanofibers to improve the mechanical and durability performance of self-healing ultra-high performance concretes exposed to aggressive waters. *Constr Build Mater.* 2023;374:130785. doi: [10.1016/j.conbuildmat.2023.130785](https://doi.org/10.1016/j.conbuildmat.2023.130785).
- [42] Wu HS, Shen AQ, Ren GP, et al. An experimental investigation and optimization of the properties of concrete containing cellulose fiber based on system theory. *Constr Build Mater.* 2024;411:134463. doi: [10.1016/j.conbuildmat.2023.134463](https://doi.org/10.1016/j.conbuildmat.2023.134463).
- [43] Wang J, Dewanckele J, Cnudde V, et al. X-ray computed tomography proof of bacterial-based self-healing in concrete. *Cem Concr Compos.* 2014;53:289–304. doi: [10.1016/j.cemconcomp.2014.07.014](https://doi.org/10.1016/j.cemconcomp.2014.07.014).
- [44] Luo M, Qian C-X, Li R-y Factors affecting crack repairing capacity of bacteria-based self-healing concrete. *Constr Build Mater.* 2015;87:1–7. doi: [10.1016/j.conbuildmat.2015.03.117](https://doi.org/10.1016/j.conbuildmat.2015.03.117).
- [45] Roig-Flores M, Moscato S, Serna P, et al. Self-healing capability of concrete with crystalline admixtures in different environments. *Constr Build Mater.* 2015;86:1–11. doi: [10.1016/j.conbuildmat.2015.03.091](https://doi.org/10.1016/j.conbuildmat.2015.03.091).
- [46] Fu T, Moon RJ, Zavattieri P, et al. Cellulose nanomaterials as additives for cementitious materials. In: Jawaid M, Boufi S, H.P.S AK, editors. *Cellulose-reinforced nanofibre composites*. United Kingdom: Woodhead Publishing; 2017. p. 455–482.
- [47] Sidiq A, Robert D, Gravina R, et al. Coupled FEM-microstructural X-ray examination of a controlled internal damage approach for concrete samples. *Archives Civ Mech Eng.* 2021;21(2):62.
- [48] Qureshi T, Kanellopoulos A, Al-Tabbaa A. Autogenous self-healing of cement with expansive minerals-I: impact in early age crack healing. *Constr Build Mater.* 2018;192:768–784. doi: [10.1016/j.conbuildmat.2018.10.143](https://doi.org/10.1016/j.conbuildmat.2018.10.143).
- [49] Wei Y, Chai J, Qin Y, et al. Effect of fly ash on mechanical properties and microstructure of cellulose fiber-reinforced concrete under sulfate dry–wet cycle attack. *Constr Build Mater.* 2021;302:124207. doi: [10.1016/j.conbuildmat.2021.124207](https://doi.org/10.1016/j.conbuildmat.2021.124207).